We are IntechOpen,
the world's leading publisher of
Open Access books
Built by scientists, for scientists

6,900
Open access books available

185,000
International authors and editors

200M
Downloads

154
Countries delivered to

Our authors are among the

TOP 1%
most cited scientists

12.2%
Contributors from top 500 universities

CLARIVATE ANALYTICS
BOOK CITATION INDEX
INDEXED

WEB OF SCIENCE™

Selection of our books indexed in the Book Citation Index
in Web of Science™ Core Collection (BKCI)

Interested in publishing with us?
Contact book.department@intechopen.com

Heat Transfer at Microscale

Mohammad Hassan Saidi and Arman Sadeghi
Center of Excellence in Energy Conversion (CEEC), School of Mechanical Engineering,
Sharif University of Technology, P.O. Box: 11155-9567, Tehran,
Iran

1. Introduction

In the past two decades, Micro-Electro-Mechanical-Systems (MEMS) have been one of the major advances of industrial technologies because of their lower cost in spite of supplying higher performance. MEMS covers micron-sized, electrically and/or mechanically driven devices. Having been derived initially from the integrated circuit (IC) fabrication technologies, MEMS devices are already emerging as products in both commercial and defense markets such as automotive, aerospace, medical, industrial process control, electronic instrumentation, office equipment, appliances, and telecommunications. Current products include: airbag crash sensors, pressure sensors, inkjet printer heads, lab-on-a-chip devices, etc. The study of microfluidics is crucial in MEMS investigations. Microfluidics may be defined as the fluid flow and heat transfer in microgeometries which by microgeometry we mean the geometries with the characteristic length scales of the order of 1-100 μm. Transport phenomena at microscale reveal many features that are not observed in macroscale devices. These features are quite different for gas and liquid flows. In gas microflows we encounter four important effects: compressibility, viscous heating, thermal creep, and rarefaction (Karniadakis et al., 2005). Liquid flows are encountered with other microscale features such as surface tension and electrokinetic effects.

This chapter deals with the fundamentals of microfluidics and major developments in this area. The flow physics pertinent to microfluidics and their methods of simulation are numerous and there is not enough space to consider all of them. Therefore, we confine our presentation to gas slip flow and electrokinetics. Section 2 is devoted to gas slip flow in microchannels with special attention to its basic concepts along with emerging features such as slip velocity, temperature jump, thermal creep, viscous dissipation, and Shear work at solid boundaries. Section 3 deals with electrokinetic phenomena such as electroosmosis and streaming potential effects.

2. Gas flow in microchannels

Design and optimization of many microdevices involve the analysis of gas flow through microchannels, as an important part of these devices. When characteristic length scale of the device is comparable with gas mean free path, continuum approach may be no longer valid, since the rarefaction effects are important. The deviation of the state of the gas from continuum behavior is measured by the Knudsen Number (Kn). For a microchannel, the

Knudsen number is defined as $Kn = \lambda/D_h$, where D_h is the channel hydraulic diameter and λ is the mean free path of gas molecules, given by $\lambda = \mu\sqrt{\pi/2RT\rho^2}$, where μ is the dynamic viscosity, R is the gas constant and T and ρ are the temperature and density of the gas, respectively (Kandlikar et al., 2006). Based on a classification given by Beskok and Karniadakis (1994), gas flow can be categorized into four regimes according to its Knudsen number. For $Kn < 10^{-3}$, the gas is considered as a continuum, while for $Kn > 10$ it is considered as a free molecular flow. In the Knudsen number ranging between 10^{-3} and 10, two different regimes exist: slip flow ($10^{-3} \leq Kn \leq 0.1$) and transition flow ($0.1 < Kn \leq 10$). In general, there are several rarefaction effects, such as discontinuities of velocity and temperature on boundary, non-Newtonian components of stress tensor, non-Fourier heat flux and formation of Knudsen boundary layer (Taheri et al., 2009). In the slip flow regime, deviations from the state of continuum are relatively small and the Navier-Stokes equations are still valid, except at the region next to the boundary which is known as Knudsen boundary layer. The Knudsen boundary layer is significant only up to distances of the order of one mean free path from the wall (Hadjiconstantinou, 2006). So, besides velocity and temperature discontinuities at the wall, its effects are negligible in slip flow regime and the Navier-Stokes equations may be applied to the whole domain. The velocity and temperature discontinuities are incorporated into the solution as boundary conditions. In the next subsection, slip flow boundary conditions along with other phenomena associated with gas flow in microchannels are introduced.

2.1 Basic concepts
2.1.1 Slip velocity and temperature jump
In this subsection, an expression for the slip velocity given by Karniadakis et al. (2005) is derived and an expression will be introduced for the temperature jump. It should be pointed out that these expressions have been originally obtained for low pressure flows and we
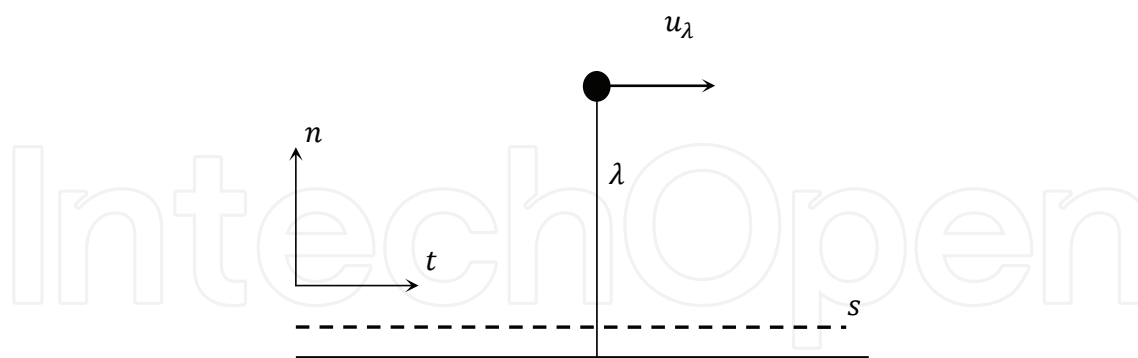

Fig. 1. Control surface for tangential momentum flux near a wall moving at velocity u_w

therefore use a similarity between fluid flow at microscale and that at low pressures. For validity of this similarity, it is necessary that the size of gas molecules be negligible compared with the characteristic length of the channel (Kandlikar et al., 2006). In slip flow regime, the minimum length scale corresponds to $Kn = 0.1$. The molecular diameter and the mean free path at atmospheric conditions for air are about 0.42 nm and 67 nm, respectively. Therefore, at $Kn = 0.1$, the characteristic length of the device is about 670 nm. So the ratio of the channel length to the gas molecular diameter is about 1595. Therefore, it seems that the

size of gas molecules is negligible compared with the characteristic length of the channel for slip flow regime and, consequently, the similarity may be used for this flow regime.

The tangential momentum flux on a surface s located near the wall shown in Fig. 1 is given by

$$\frac{1}{4}n_s m \bar{v} u_s \tag{1}$$

in which n_s is the number density of the molecules crossing surface s, m is the molecular mass, u_s is the tangential (slip) velocity of the gas on this surface, and $\bar{v}$ is the mean thermal speed given by (Kennard, 1938)

$$\bar{v} = (8RT/\pi)^{0.5} \tag{2}$$

We now assume that approximately half of the molecules passing through s are coming from a layer of gas at a distance proportional to one mean free path away from the surface. The tangential momentum flux of these incoming molecules is written as

$$\frac{1}{4}n_\lambda m \bar{v}_\lambda u_\lambda \tag{3}$$

where the subscript λ indicates quantities evaluated one mean free path away from the surface. Since we have assumed that half of the molecules passing through s are coming from λ away from this surface, therefore $n_\lambda = \frac{1}{2}n_s$. The other half of the molecules passing through s are reflected from the wall with a tangential momentum flux of

$$\frac{1}{4}n_w m \bar{v}_w u_r \tag{4}$$

where the subscript w indicates wall conditions, u_r shows the average tangential velocity of the molecules reflected from the wall, and the number density n_w is equal to $\frac{1}{2}n_s$. For determination of u_r, the definition of tangential momentum accommodation coefficient, F_m, should be used. Assuming that F_m fraction of the molecules are reflected from the wall with average tangential velocity corresponding to that of the wall, u_w, and $(1 - F_m)$ of the molecules are reflected from the wall conserving their average incoming tangential velocity, u_λ, we have

$$u_r = F_m u_w + (1 - F_m)u_\lambda \tag{5}$$

Therefore, the total tangential momentum flux on surface s is given by

$$\frac{1}{4}n_s m \bar{v} u_s = \frac{1}{4}n_\lambda m \bar{v}_\lambda u_\lambda + \frac{1}{4}n_w m \bar{v}_w [F_m u_w + (1 - F_m)u_\lambda] \tag{6}$$

We now assume that the temperatures of the fluid and the surface are the same. So the mean thermal speeds become identical, i.e., $\bar{v}_s = \bar{v}_\lambda = \bar{v}_w$. By applying the aforementioned assumptions to the above equation, the slip velocity, u_s, is obtained as follows

$$u_s = \frac{1}{2}[u_\lambda + (1 - F_m)u_\lambda + F_m u_w] \tag{7}$$

Using a Taylor series expansion for u_λ about u_s, results in

$$u_s = \frac{1}{2}\left[u_s + \lambda\left(\frac{\partial u}{\partial n}\right)_s + \frac{\lambda^2}{2}\left(\frac{\partial^2 u}{\partial n^2}\right)_s + \cdots\right]$$
$$+ \frac{1}{2}\left\{(1 - F_m)\left[u_s + \lambda\left(\frac{\partial u}{\partial n}\right)_s + \frac{\lambda^2}{2}\left(\frac{\partial^2 u}{\partial n^2}\right)_s + \cdots\right] + F_m u_w\right\} \qquad (8)$$

where n is the normal direction exiting the wall. This expansion ultimately results in the following slip relation on the boundaries

$$u_s - u_w = \frac{2 - F_m}{F_m}\left[\lambda\left(\frac{\partial u}{\partial n}\right)_s + \frac{\lambda^2}{2}\left(\frac{\partial^2 u}{\partial n^2}\right)_s + \cdots\right] \qquad (9)$$

The above relation may be written dimensionless based on appropriate scale velocity and reference length as

$$u_s^* - u_w^* = \frac{2 - F_m}{F_m}\left[Kn\left(\frac{\partial u^*}{\partial n^*}\right)_s + \frac{Kn^2}{2}\left(\frac{\partial^2 u^*}{\partial n^{*2}}\right)_s + \cdots\right] \qquad (10)$$

If we truncate the above equation to include only up to first order terms in Kn, we recover Maxwell's first order slip boundary condition (Maxwell, 1879)

$$u_s^* - u_w^* = \frac{2 - F_m}{F_m}Kn\left(\frac{\partial u^*}{\partial n^*}\right)_s \qquad (11)$$

Karniadakis et al. (2005) have proposed the following general slip velocity, instead of Eq. (11)

$$u_s^* - u_w^* = \frac{2 - F_m}{F_m}\frac{Kn}{1 - bKn}\left(\frac{\partial u^*}{\partial n^*}\right)_s \qquad (12)$$

where b is a general slip coefficient. The value of b is determined such that maximum agreement between the calculated velocity profiles with Direct Simulation Monte Carlo (DSMC) results is obtained. For channel flow, it has been shown that $b = -1$ provides more accurate results. The above equations exclude the thermal creep effects, since they have been obtained based on isothermal condition. We will add the corresponding term due to the thermal creep to the above equation in the next sections.

For the temperature jump, the following expression is given by Kennard (1938) which is obtained based on the kinetic theory of gases

$$T_s^* - T_w^* = \frac{2 - F_t}{F_t}\frac{2\gamma}{1 + \gamma}\frac{Kn}{Pr}\left(\frac{\partial T^*}{\partial n^*}\right)_s \qquad (13)$$

in which F_t is the thermal accommodation coefficient, γ is the specific heat capacity ratio, and Pr is the Prandtl number. Karniadakis et al. (2005) proposed the following form for the high order temperature jump condition by analogy with Eq. (10)

$$T_s^* - T_w^* = \frac{2 - F_t}{F_t}\frac{2\gamma}{1 + \gamma}\frac{1}{Pr}\left[Kn\left(\frac{\partial T^*}{\partial n^*}\right)_s + \frac{Kn^2}{2}\left(\frac{\partial^2 T^*}{\partial n^{*2}}\right)_s + \cdots\right] \qquad (14)$$

2.1.2 Thermal creep

The term thermal creep points out to rarefied gas flow due to tangential temperature gradients along the channel walls, where the fluid starts creeping in the direction from cold

towards hot. This phenomenon may be explained by means of the following example used by Karniadakis et al. (2005): Let us consider two containers filled with the same gas that are kept at the same pressure

$$P_1 = P_2 \tag{15}$$

but at different temperatures

$$T_1 > T_2 \tag{16}$$

It is now assumed that these two containers are connected with a relatively thin channel having the height of $H \ll \lambda$. In this situation, the intermolecular collisions are negligible compared with the interaction of molecules with the surfaces of the channel. Then, the assumption of $F_m = 0$ will result in the validation of the following analysis. It is assumed that the density of the fluid is proportional to the number density

$$\rho \propto n \tag{17}$$

and the temperature of the fluid is proportional to the square of average molecular speed, $\bar{c}$

$$T \propto \bar{c}^2 \tag{18}$$

The mass fluxes at the hot and the cold ends of the channel are $mn_1\bar{c}_1$ and $mn_2\bar{c}_2$, respectively, with m being the mass of the gas molecules. Then

$$\frac{mn_1\bar{c}_1}{mn_2\bar{c}_2} \approx \frac{\rho_1}{\rho_2}\left(\frac{T_1}{T_2}\right)^{0.5} = \frac{P_1}{P_2}\left(\frac{T_2}{T_1}\right)^{0.5} = \left(\frac{T_2}{T_1}\right)^{0.5} \leq 1 \tag{19}$$

in which the equation of state of ideal gas has been used, i.e.,

$$P = \rho R T \tag{20}$$

The above analysis indicates a flow creeping from cold to hot. A detailed derivation of thermal creep boundary condition is given by Kennard (1938) and the resultant velocity which should be added to Eq. (9) is as follows

$$u_c = \frac{3}{4}\frac{\mu R}{P}\left(\frac{\partial T}{\partial t}\right)_s \tag{21}$$

where u_c is the creep velocity, and $(\partial T/\partial t)_s$ is the tangential temperature gradient along the surface. Using the equation of state of ideal gas and the relation $\lambda = \mu\sqrt{\pi/2RT\rho^2}$, Eq. (21) may be written as

$$u_c = \frac{3}{2\pi}\frac{R\rho\lambda^2}{\mu}\left(\frac{\partial T}{\partial t}\right)_s \tag{22}$$

and in dimensionless form as

$$u_c^* = \frac{3}{2\pi}\frac{\gamma - 1}{\gamma}\frac{ReKn^2}{Ec}\left(\frac{\partial T^*}{\partial t^*}\right)_s \tag{23}$$

in which $Re = \rho U D_h/\mu$ and $Ec = U^2/c_p\Delta T$ with U and ΔT being the reference velocity and temperature difference. Therefore, the complete expression for the slip velocity may be written as

$$u_s^* - u_w^* = \frac{2 - F_m}{F_m}\left[Kn\left(\frac{\partial u^*}{\partial n^*}\right)_s + \frac{Kn^2}{2}\left(\frac{\partial^2 u^*}{\partial n^{*2}}\right)_s + \cdots\right] + \frac{3}{2\pi}\frac{\gamma - 1}{\gamma}\frac{ReKn^2}{Ec}\left(\frac{\partial T^*}{\partial t^*}\right)_s \tag{24}$$

2.1.3 Viscous dissipation

Viscous dissipation effects are typically only significant for high viscous flows or in presence of high gradients in velocity distribution. In macroscale, such high gradients occur in high velocity flows. In microscale devices, however, because of small dimensions, such high gradients may occur even for low velocity flows. So, for microchannels the viscous dissipation should be taken into consideration. Viscous dissipation features as a source term in the fluid flow due to the conversion of the kinetic motion of the fluid to the thermal energy and causes variation in the temperature distribution. The effects of viscous dissipation on the temperature field and ultimately on the friction factor have been investigated by Koo and Kleinstreuer (2003, 2004), using dimensional analysis and experimentally validated computer simulations. It was found that ignoring viscous dissipation could affect accurate flow simulations and measurements in microconduits. The effect of viscous dissipation in convective heat transfer is characterized by the Brinkman number, Br, which is the ratio of energy generated by viscous heating to the energy transferred by conduction at the solid boundaries, i.e.,

$$Br = \frac{\mu U^2}{qH} \quad \text{or} \quad Br = \frac{\mu U^2}{k\Delta T} \tag{25}$$

where q is the wall heat flux and H is the channel height or radius. Some theoretical studies has been undertaken to investigate viscous dissipation effects on the heat transfer features of the gas flow in microchannels of different cross section such as circular channel (Aydin and Avci, 2006), parallel plate and annular channel (Sadeghi and Saidi, 2010), and rectangular channel (Rij et al., 2009).

2.1.4 Flow work and shear work at solid boundaries

In this section, we discuss the effects of flow work and shear work at the boundary in slip flow and how these affect convective heat transfer in small scale channels. Flow work and shear work at the boundary have been neglected in the majority of the recent studies of viscous dissipation in slip flow convective heat transfer. However, flow work is of the same order of magnitude as viscous dissipation (Ou and Cheng, 1973). Also Hadjiconstantinou (2003) showed that, for rarefied flows, the effect of shear work scales with the Brinkman number. The effect of shear work on boundary is due to the slip velocity and it is zero at macroscale. This effect causes smaller amounts of the streamwise temperature gradient at slip flow regime. Therefore, in order to take it into account, one should consider its effects in evaluating the axial temperature gradient. Let us show the effects of shear work by considering the fully developed slip flow forced convection in a parallel plate microchannel with the channel half height of H, which is shown in Fig. 2.

The energy equation including the effects of viscous dissipation and flow work is written as

$$\rho c_p u \frac{\partial T}{\partial x} = k\frac{\partial^2 T}{\partial y^2} + u\frac{dP}{dx} + \tau_{xy}\frac{du}{dy} \tag{26}$$

In the above equation, $u\,dP/dx$ and $\tau_{xy}\,du/dy$ denote the rate of energy absorbed by flow work and generated by viscous heating, respectively. It is noteworthy that for a constant

wall heat flux, which is the case in this example, the axial conduction term in the energy equation is zero. The integral form of the above equation in the transverse direction becomes

$$\rho c_p UH \frac{dT_b}{dx} = q + UH \frac{dP}{dx} + \int_0^H \tau_{xy} \frac{du}{dy} dy \qquad (27)$$

in which q is the thermal energy transferred from the wall to the fluid, U is the mean velocity, and T_b is the bulk temperature defined as
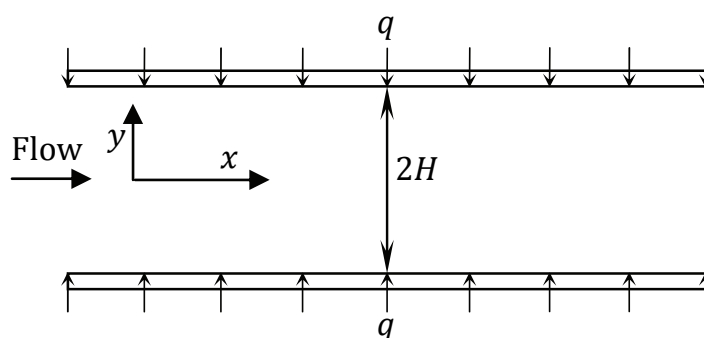
$$T_b = \frac{\int_0^H uT dy}{UH} \qquad (28)$$

Fig. 2. Schematic of a parallel plate microchannel with coordinate system

In addition to the thermal energy transfer, there is also dissipation due to shear work between the wall and the slipping gas. It is the sum of these two contributions that is responsible for the axial temperature gradient as shown by the integral form of the total (mechanical plus thermal) energy equation (Hadjiconstantinou, 2003)

$$\rho c_p UH \frac{dT_b}{dx} = q + u_s \tau_{xy,s} \qquad (29)$$

in which u_s is the slip velocity and $\tau_{xy,s} = \mu (du/dy)_s$ is the wall shear stress. In Eq. (29), $u_s \tau_{xy,s}$ is the dissipation due to shear work between the wall and the slipping gas and it is zero at no slip condition. Equations (27) and (29) are linked by the mechanical energy balance

$$0 = -u \frac{dP}{dx} + u \frac{d\tau_{xy}}{dy} = -u \frac{dP}{dx} + \frac{d(u\tau_{xy})}{dy} - \tau_{xy} \frac{du}{dy} \qquad (30)$$

which integrates to

$$u_s \tau_{xy,s} = UH \frac{dP}{dx} + \int_0^H \tau_{xy} \frac{du}{dy} dy \qquad (31)$$

and shows that the viscous heating and flow work terms in Eq. (27) are, in effect, representing the contribution of the shear work at the wall. Hadjiconstantinou (2003) obtained the Nusselt number based on the total heat exchange between the wall and the flow, Nu_t, as

$$Nu_t = Nu + \frac{4Hu_s\tau_{xy,s}}{k(T_w - T_b)} \tag{32}$$

with $Nu = 4Hq/k(T_w - T_b)$ being the Nusselt number based on the thermal energy exchange. In spite of their importance, the effects of flow work and shear work at boundaries have rarely been investigated in the literature. The only work performed is by Rij et al (2009) which numerically investigated slip flow forced convection in rectangular microchannels.

2.2 Slip flow forced convection

In this section, we consider slip flow forced convection in microchannels. First, a solution is derived for forced convection with viscous dissipation in a parallel plate microchannel and, afterwards, the other progresses in the literature will shortly be presented. Let us consider fully developed forced convection in a parallel plate microchannel with constant wall heat fluxes which was shown in Fig. 2. The momentum equation in x-direction and relevant boundary conditions may be written as

$$\frac{\mathrm{d}^2 u}{\mathrm{d}y^2} = \frac{1}{\mu}\frac{\mathrm{d}p}{\mathrm{d}z} = \text{const.}$$

$$u_{(H)} = -\frac{2 - F_m}{F_m} Kn D_h \left(\frac{\mathrm{d}u}{\mathrm{d}y}\right)_{(H)} \qquad \text{and} \qquad \left(\frac{\mathrm{d}u}{\mathrm{d}y}\right)_{(0)} = 0 \tag{33}$$

here $D_h = 4H$. The dimensionless velocity distribution will then be

$$u^* = \frac{3}{2}\left(\frac{1 - y^{*2} + 8\dfrac{2 - F_m}{F_m}Kn}{1 + 12\dfrac{2 - F_m}{F_m}Kn}\right) \tag{34}$$

in which $y^* = y/H$, $u^* = u/U$ and U is the mean velocity.

The energy equation including the effects of viscous dissipation and relevant boundary conditions are written as

$$u\frac{\partial T}{\partial z} = \alpha\frac{\partial^2 T}{\partial y^2} + \frac{v}{c_p}\left(\frac{\mathrm{d}u}{\mathrm{d}y}\right)^2$$

$$T_{(x,H)} - T_w = -\frac{2 - F_t}{F_t}\frac{8\gamma}{1 + \gamma}\frac{KnH}{Pr}\left(\frac{\partial T}{\partial y}\right)_{(x,H)} \qquad \text{and} \qquad \left(\frac{\partial T}{\partial y}\right)_{(x,0)} = 0 \tag{35}$$

We introduce dimensionless temperature as follows, which only depends on y for fully developed flow

$$\theta(y) = \frac{T - T_s}{\dfrac{qH}{k}} \tag{36}$$

in which T_s is the gas temperature at the wall. Taking differentiation of Eq. (36) with respect to x gives

$$\frac{\partial T}{\partial x} = \frac{dT_s}{dx} = \frac{dT_b}{dx} \tag{37}$$

From an energy balance on a length of duct dx, the following expression is obtained for dT_b/dx

$$\frac{dT_b}{dx} = \frac{q}{\rho c_p U H}\left[1 + \frac{12Br}{\left(1 + 12\frac{2 - F_m}{F_m}Kn\right)^2}\right] \tag{38}$$

in which $Br = \mu U^2/4qH$. The energy equation then is modified into the following dimensionless form

$$\frac{d^2\theta}{dy^{*2}} = a - by^{*2} \tag{39}$$

with the following coefficients

$$a = \frac{3(1 + 8\frac{2 - F_m}{F_m}Kn)}{2\left(1 + 12\frac{2 - F_m}{F_m}Kn\right)}\left[1 + \frac{12Br}{\left(1 + 12\frac{2 - F_m}{F_m}Kn\right)^2}\right]$$

$$\tag{40}$$

$$b = \frac{3}{2\left(1 + 12\frac{2 - F_m}{F_m}Kn\right)} + \frac{36Br}{\left(1 + 12\frac{2 - F_m}{F_m}Kn\right)^2} + \frac{18Br}{\left(1 + 12\frac{2 - F_m}{F_m}Kn\right)^3}$$

The thermal boundary conditions in the dimensionless form are written as

$$\left(\frac{d\theta}{dy^*}\right)_{(0)} = 0 \quad , \quad \theta_{(1)} = 0 \tag{41}$$

Using Eq. (39) and applying boundary conditions (41), the dimensionless temperature distribution is obtained as

$$\theta(y^*) = -\frac{a}{2}\left(1 - y^{*2}\right) + \frac{b}{12}\left(1 - y^{*4}\right) \tag{42}$$

On the other hand, Eq. (42) which is in terms of T_s can be transformed into an equation in terms of T_w, using the following conversion formula

$$\frac{T_w - T_s}{\frac{qH}{k}} = \frac{2 - F_t}{F_t}\frac{8\gamma}{1 + \gamma}\frac{Kn}{Pr} \tag{43}$$

So that Eq. (42) becomes

$$\theta^*(y^*) = \frac{T - T_w}{\frac{qH}{k}} = \frac{T - T_s}{\frac{qH}{k}} - \frac{T_w - T_s}{\frac{qH}{k}} = -\frac{a}{2}\left(1 - y^{*2}\right) + \frac{b}{12}\left(1 - y^{*4}\right) - \frac{2 - F_t}{F_t}\frac{8\gamma}{1 + \gamma}\frac{Kn}{Pr} \tag{44}$$

To obtain the Nusselt number, first the dimensionless bulk temperature θ_b^* must be calculated, which is given by

$$\theta_b^* = \frac{\int_0^1 u^* \theta^* \mathrm{d}y^*}{\int_0^1 u^* \mathrm{d}y^*} = \frac{3}{4\left(1 + 12\frac{2 - F_m}{F_m}Kn\right)}\left[\left(1 + 8\frac{2 - F_m}{F_m}Kn\right)\left(2 - \frac{8}{3}a + \frac{4}{5}b\right) - \frac{2}{3} + \frac{4}{5}a \right.$$
$$\left. - \frac{16}{63}b\right] - \frac{2 - F_t}{F_t}\frac{8\gamma}{1 + \gamma}\frac{Kn}{Pr} \tag{45}$$

Based on definition, the Nusselt number is written as

$$Nu = \frac{hD_h}{k} = \frac{qD_h}{k(T_w - T_b)} = -\frac{4}{\theta_b^*} \tag{46}$$

Some of the results obtained for this example are now depicted using $F_m = F_t = 1$. Figure 3 depicts transverse distribution of dimensionless velocity at different values of Knudsen number. As a result of slip conditions, slip velocities occur at the walls. An increase in Kn results in an increase in the slip velocities at the walls, while according to mass conservation, the maximum velocity decreases. Note that as Knudsen number increases the velocity gradient becomes smaller, especially at the walls at which the maximum decrease occurs.
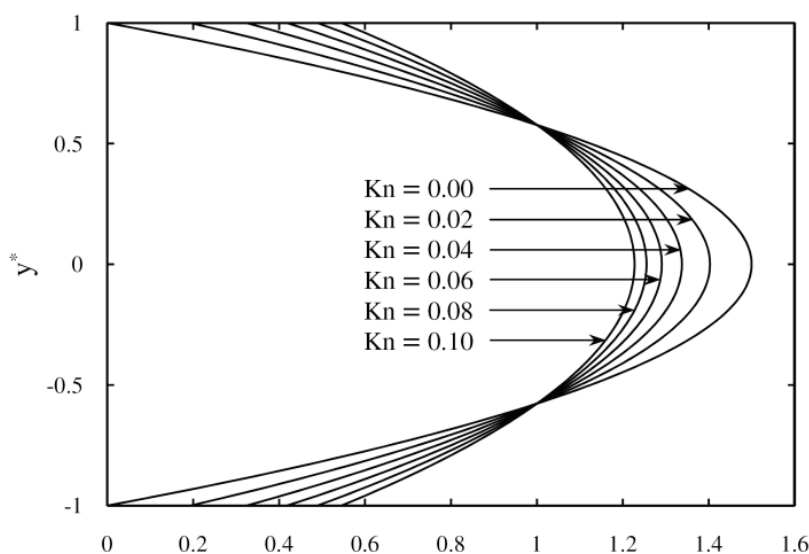

Fig. 3. Transverse distribution of dimensionless velocity at different values of Knudsen number

The effect of rarefaction on dimensionless temperature profile is illustrated in Fig. 4. As observed, to increase Knudsen number is to decrease dimensionless temperature as a result of temperature jump at the wall.

Figure 5 illustrates the Nusselt number values versus Knudsen number at different Brinkman numbers. Both positive and negative values of the heat fluxes at the walls are considered. Positive values of Brinkman number correspond to the wall cooling case where heat is transferred from the walls to the fluid, while the opposite is true for negative values of Brinkman number. For each case, the viscous dissipation behaves like an energy source increasing the temperature of the fluid especially near the wall since the highest shear rate occurs at this region while it is zero at the centerline. In the absence of viscous dissipation, the distribution of dimensionless temperature is independent of whether the wall is heated or cooled. As seen, for wall cooling case, which corresponds to positive values of Brinkman number, viscous dissipation decreases the Nusselt number. Viscous heating increases the

difference between the wall and the bulk temperatures. Thus for a constant value of wall heat flux, according to Eq. (46), the Nusselt number values decrease. For wall heating case, as expected, viscous heating leads to greater values of Nusselt number. Increasing values of Knudsen number result in decreasing the values of Nusselt number for wall cooling case and also for no viscous heating case. But for wall heating case at small values of Knudsen number, an increment of Knudsen number values leads to a larger amount of Nusselt, while the opposite is true for larger values of Knudsen. For all cases, the effect of Brinkman number on Nusselt number becomes insignificant at larger values of Knudsen number. This is due to the fact that the slip velocity tends to unify the velocity profile which leads to smaller velocity gradients and consequently smaller shear rates, which in the following reduces viscous heating effects.
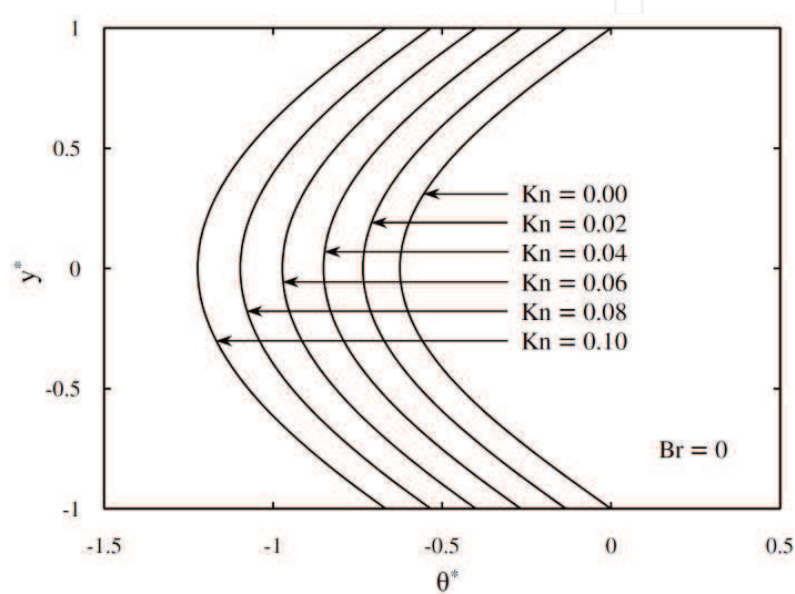

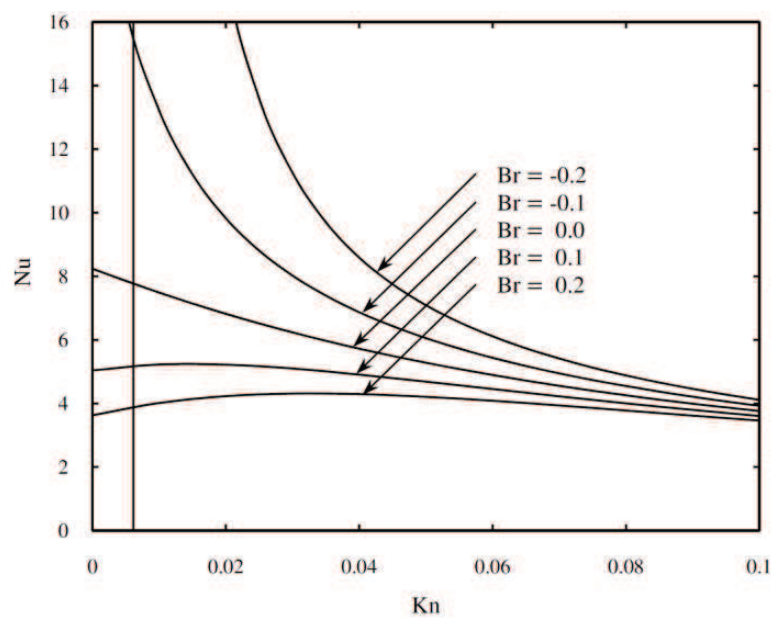Fig. 4. Effect of rarefaction on dimensionless temperature profile for no viscous heating case

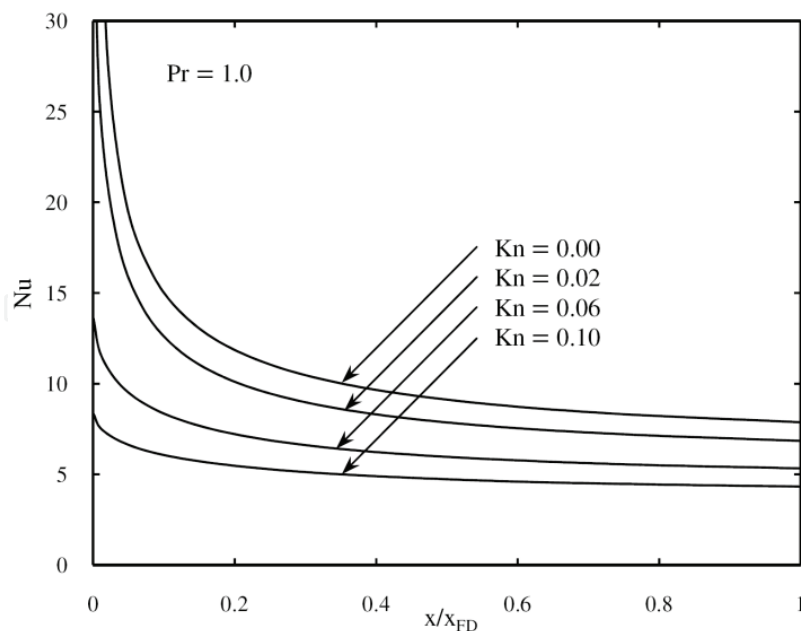Fig. 5. Nusselt number values versus Knudsen number at different Brinkman numbers

Fig. 6. Nusselt number in the entrance region for different Knudsen numbers (Sadeghi et al., 2009)

Slip flow forced convection in microchannels has widely been investigated in the literature. Aydin and Avci (2006, 2007) analytically studied fully developed laminar slip flow forced convection in a micropipe and microchannel between two parallel plates. The thermally developing cases have been studied by Jeong and Jeong (2006a, 2006b) by taking the effects of viscous dissipation and streamwise conduction into account. Fully developed laminar slip flow forced convection in a rectangular microchannel was studied by Tunc and Bayazitoglu (2002), using integral transform method. The thermally developing case has been studied by Yu and Ameel (2001) by applying a modified generalized integral transform technique to solve the energy equation, assuming hydrodynamically fully developed flow. Sadeghi et al. (2009) have performed a boundary layer analysis for simultaneously developing flow through parallel plate microchannels with constant wall temperatures. The results showed that an increment in Knudsen number leads to a larger amount of hydrodynamic entry length. They proposed the following correlation for Nusselt number in the entrance region

$$Nu = 3 \left\{ \frac{\delta}{D} + \frac{6\gamma}{1+\gamma}\frac{Kn}{Pr} - \frac{\left(3Kn + \frac{19}{60}\frac{\delta}{D}\right)\left(\frac{\delta}{D}\right)^2}{\left[8Kn\frac{\delta}{D} + \frac{4}{3}\left(\frac{\delta}{D}\right)^2 + \left(1 - 2\frac{\delta}{D}\right)\left(4Kn + \frac{\delta}{D}\right)\right]} \right\}^{-1} \tag{47}$$

where D is the channel width and δ is the boundary layer thickness. Figure 6 depicts the above correlation for different Knudsen numbers at $Pr = 1$. It can be seen that the effects of rarefaction are more significant at the inlet.

2.3 Slip flow free convection
In comparison with forced convection, much less attention has been given to free convection slip flow in the literature. The first work in this field has been done by Chen and Weng

(2005), which analytically studied fully developed natural convection in an open-ended vertical parallel plate microchannel with asymmetric wall temperature distributions. They showed that the Nusselt number based on the channel width is given by

$$Nu = \frac{1 - \dfrac{T_2 - T_0}{T_1 - T_0}}{1 + 2\dfrac{2 - F_t}{F_t}Kn} \qquad (48)$$

where T_1 and T_2 are the wall temperatures and T_0 is the free stream temperature. Chen and Weng afterwards extended their works by taking the effects of thermal creep (2008a) and variable physical properties (2008b) into account. Natural convection gaseous slip flow in a vertical parallel plate microchannel with isothermal wall conditions was numerically investigated by Biswal et al. (2007), in order to analyze the influence of the entrance region on the overall heat transfer characteristics. Chakraborty et al. (2008) performed a boundary layer integral analysis to investigate the heat transfer characteristics of natural convection gas flow in symmetrically heated vertical parallel plate microchannels. It was revealed that for low Rayleigh numbers, the entrance length is only a small fraction of the total channel extent.

2.4 Thermal creep effects

When the channel walls are subject to constant temperature, the thermal creep effects vanish at the fully developed conditions. However, for a constant heat flux boundary condition, the effects of thermal creep may become predominant for small Eckert numbers.
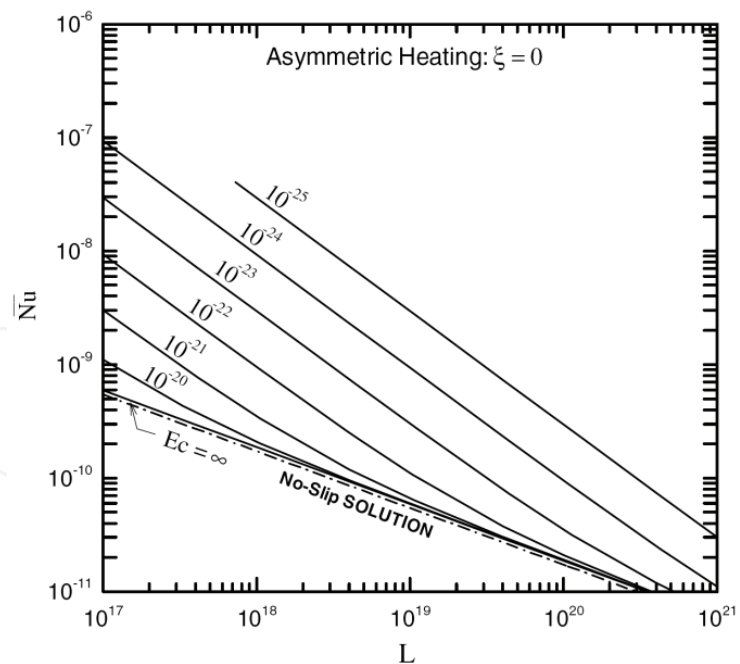

Fig. 7. Variation of average Nusselt number as a function of the channel length, L, for different values of Ec with $Kn = 0.03$ (Chen and Weng, 2008a)

The effects of thermal creep for parallel plate and rectangular microchannels have been investigated by Rij et al. (2007) and Niazmand et al. (2010), respectively. As mentioned before, Chen and Weng (2008a) studied the effects of creep flow in steady natural

convection in an open-ended vertical parallel plate microchannel with asymmetric wall heat fluxes. It was found that the thermal creep has a significant effect which is to unify the velocity and pressure and to elevate the temperature. Moreover, the effect of thermal creep was found to be enhancing the flow rate and heat transfer rate and reducing the maximum gas temperature and flow drag. Figure 7 shows the variation of average Nusselt number as a function of the channel length, L, for different values of Ec with $Kn = 0.03$. Note that ξ is the ratio of the wall heat fluxes. It can be seen that the thermal creep significantly increases the average Nusselt number.

3. Electrokinetics

In this section, we pay attention to electrokinetics. Electrokinetics is a general term associated with the relative motion between two charged phases (Masliyah and Bhattacharjee, 2006). According to Probstein (1994), the electrokinetic phenomena can be divided into the following four categories

- *Electroosmosis* is the motion of ionized liquid relative to the stationary charged surface by an applied electric field.
- *Streaming potential* is the electric field created by the motion of ionized fluid along stationary charged surfaces.
- *Electrophoresis* is the motion of the charged surfaces and macromolecules relative to the stationary liquid by an applied electric field.
- *Sedimentation potential* is the electric field created by the motion of charged particles relative to a stationary liquid.

Due to space limitations, only the first two effects are being considered here. The study of electrokinetics requires a basic knowledge of electrostatics and electric double layer. Therefore, the next section is devoted to these basic concepts.

3.1 Basic concepts
3.1.1 Electrostatics

Consider two stationary point charges of magnitude Q_1 and Q_2 in free space separated by a distance R. According to the Coulomb's law the mutual force between these two charges, $\mathbf{F}_{12}$, is given by

$$\mathbf{F}_{12} = \frac{Q_1 Q_2}{4\pi\varepsilon_0 R^2} \mathbf{r}_{12} \tag{49}$$

in which $\mathbf{r}_{12}$ is a unit vector directed from Q_1 towards Q_2. Here, ε_0 is the permittivity of vacuum which its value is $8.854 \times 10^{-12} \text{CV}^{-1}\text{m}^{-1}$ with C (Coulomb) being the SI unit of electric charge. The electric field $\mathbf{E}$ at a point in space due to the point charge Q is defined as the electric force $\mathbf{F}$ acting on a positive test charge Q_t placed at that point divided by the magnitude of the test charge, i.e.,

$$\mathbf{E} = \frac{\mathbf{F}}{Q_t} = \frac{Q}{4\pi\varepsilon_0 R^2} \mathbf{r} \tag{50}$$

where $\mathbf{r}$ is a unit vector directed from Q towards Q_t. One can generalize Eq. (50) by replacing the discrete point charge by a continuous charge distribution. The electric field then becomes

$$\mathbf{E} = \frac{1}{4\pi\varepsilon_0} \int \frac{\mathrm{d}\rho_e}{R^2}\mathbf{r} \tag{51}$$

where the integration is over the entire charge distribution and ρ_e is the electrical charge density which may be per line, surface, or volume.

Let us pay attention to the Gauss's law, a useful tool which relates the electric field strength flux through a closed surface to the enclosed charge. To derive the Gauss's law, we consider a point charge Q located in some arbitrary volume, V, bounded by a surface S as shown in Fig. 8.
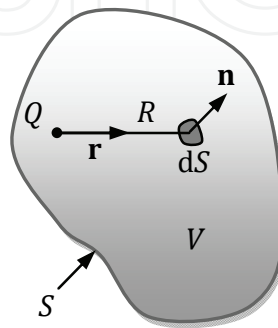
Fig. 8. Point charge Q bounded by a surface S.

The electric field strength at the element of surface $\mathrm{d}S$ due to the charge Q is given by

$$\mathbf{E} = \frac{Q}{4\pi\varepsilon_0 R^2}\mathbf{r} \tag{52}$$

where the unit vector $\mathbf{r}$ is directed from the point charge towards the surface element $\mathrm{d}S$. Performing dot product for Eq. (52) using $\mathbf{n}\mathrm{d}S$ with $\mathbf{n}$ being the unit outward normal vector to the bounding surface and integrating over the bounding surface S, we come up with

$$\oint_S (\mathbf{E}\cdot\mathbf{n})\mathrm{d}S = \oint_S \frac{Q}{4\pi\varepsilon_0 R^2}(\mathbf{r}\cdot\mathbf{n})\mathrm{d}S \tag{53}$$

The term $(\mathbf{r}\cdot\mathbf{n})\mathrm{d}S/R^2$ represents the element of solid angle $\mathrm{d}\Omega$. Therefore, the above equation becomes

$$\oint_S (\mathbf{E}\cdot\mathbf{n})\mathrm{d}S = \frac{1}{4\pi\varepsilon_0}\int_0^{4\pi} Q\mathrm{d}\Omega \tag{54}$$

Upon integration, Eq. (54) gives

$$\oint_S (\mathbf{E}\cdot\mathbf{n})\mathrm{d}S = \frac{Q}{\varepsilon_0} \tag{55}$$

Equation (55) is the integral form of the Gauss's law or theorem. The differential form of the Gauss's law can be derived quite readily using the divergence theorem, which states that

$$\int_S (\mathbf{E}\cdot\mathbf{n})\mathrm{d}S = \int_V (\nabla\cdot\mathbf{E})\mathrm{d}V \tag{56}$$

and the total charge Q may be written based on the charge density as

$$Q = \int_V \rho_e \mathrm{d}V \tag{57}$$

The following equation is obtained, using Eqs. (55) to (57)

$$\int_V (\nabla \cdot \mathbf{E}) \mathrm{d}V = \frac{1}{\varepsilon_0} \int_V \rho_e \mathrm{d}V \tag{58}$$

Since the volume V is arbitrary, therefore

$$\nabla \cdot \mathbf{E} = \frac{\rho_e}{\varepsilon_0} \tag{59}$$

The above is the differential form of the Gauss's law.
Using Eq. (50), it is rather straightforward to show that

$$\nabla \times \mathbf{E} = 0 \tag{60}$$

From the above property, it may be considered that the electric field is the gradient of some scalar function, ψ, known as electric potential, i.e.,

$$\mathbf{E} = -\nabla \psi \tag{61}$$

By substituting the electric field from Eq. (61) into Eq. (59), we come up with the Poison equation:

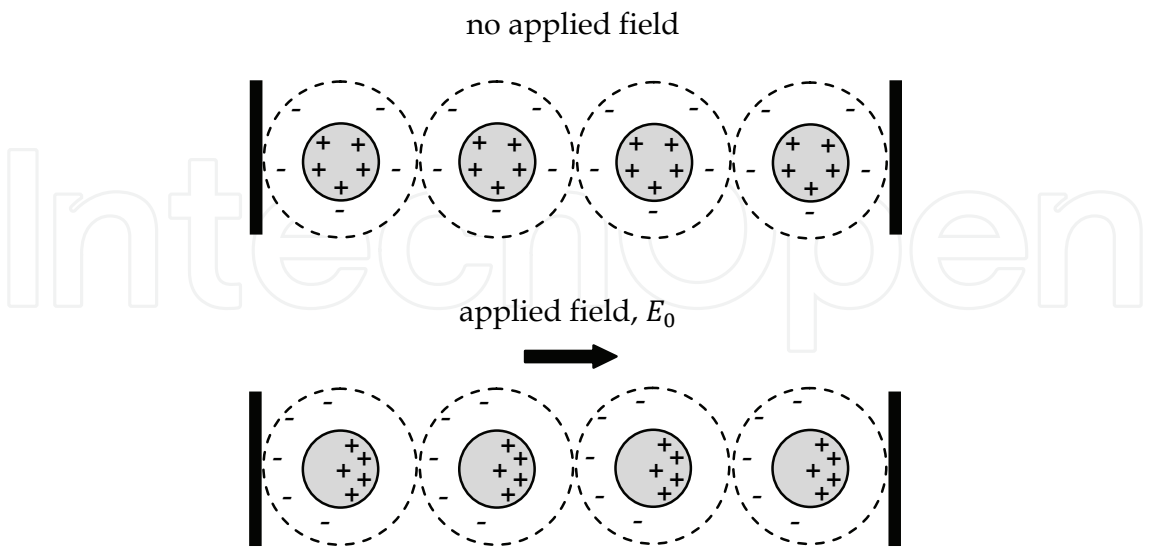$$\nabla^2 \psi = -\frac{\rho_e}{\varepsilon_0} \tag{62}$$

Fig. 9. Polarization of a dielectric material in presence of an electric field

All the previous results are pertinent to the free space and are not useful for practical applications. Therefore, we should modify them by taking into account the materials

electrical properties. It is worth mentioning that from the perspective of classical electrostatics, the materials are broadly categorized into two classes, namely, conductors and dielectrics. Conductors are materials that contain free electric charges. When an electrical potential difference is applied across such conducting materials, the free charges will move to the regions of different potentials depending on the type of charge they carry. On the other hand, dielectric materials do not have free or mobile charges. When a dielectric is placed in an electric field, electric charges do not flow through the material, as in a conductor, but only slightly shift from their average equilibrium positions causing dielectric polarization. Because of dielectric polarization, positive charges are displaced toward the field and negative charges shift in the opposite direction. This creates an internal electric field that partly compensates the external field inside the dielectric. The mechanism of polarization is schematically shown in Fig. 9.
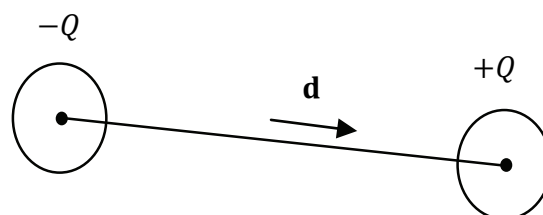

Fig. 10. Schematic of a dipole.

We should now derive the relevant electrostatic equations for a dielectric medium. In the presence of an electric field, the molecules of a dielectric material constitute dipoles. A dipole, which is shown in Fig. 10, comprises two equal and opposite charges, $+Q$ and $-Q$, separated by a distance d. Dipole moment, a vector quantity, is defined as $Q\mathbf{d}$, where $\mathbf{d}$ is the vector orientation between the two charges. The polarization density, $\mathbf{P}$, is defined as the dipole moment per unit volume. It is thus given by

$$\mathbf{P} = NQ\mathbf{d} \tag{63}$$

where N is the number of dipoles per unit volume. For homogeneous, linear, and isotropic dielectric medium, when the electric field is not too strong, the polarization is directly proportional to the applied field, and one can write

$$\mathbf{P} = \chi \varepsilon_0 \mathbf{E} \tag{64}$$

Here χ is a dimensionless parameter known as electric susceptibility of the dielectric medium. The following relation exists between the polarization density and the volumetric polarization (or bound) charge density, ρ_p

$$\nabla \cdot \mathbf{P} = -\rho_p \tag{65}$$

Within a dielectric material, the total volumetric charge density is made up of two types of charge densities, a polarization and a free charge density

$$\rho_e = \rho_p + \rho_f \tag{66}$$

One can combine the definition of total charge density provided by Eq. (66) with the Gauss's law, Eq. (59), to get

$$\nabla \cdot \mathbf{E} = \frac{1}{\varepsilon_0}(\rho_p + \rho_f) \tag{67}$$

By substituting the polarization charge, from Eq. (65), the divergence of the electric field becomes

$$\nabla \cdot \mathbf{E} = \frac{1}{\varepsilon_0}(\nabla \cdot \mathbf{P} + \rho_f) \tag{68}$$

which may be rearranged as

$$\nabla \cdot (\varepsilon_0 \mathbf{E} + \mathbf{P}) = \rho_f \tag{69}$$

The polarization may be substituted from Eq. (64) and the outcome is the following

$$\nabla \cdot [\varepsilon_0(1 + \chi)\mathbf{E}] = \rho_f \tag{70}$$

Let

$$\varepsilon = \varepsilon_0(1 + \chi) \tag{71}$$

We will call ε the permittivity of the material. Therefore, Eq. (70) becomes

$$\nabla \cdot (\varepsilon \mathbf{E}) = \rho_f \tag{72}$$

For constant permittivity, Eq. (72) gives

$$\varepsilon \nabla \cdot \mathbf{E} = \rho_f \tag{73}$$

which is Maxwell's equation for a dielectric material. Equation (73) may be written as

$$\varepsilon_0 \varepsilon_r \nabla \cdot \mathbf{E} = \rho_f \tag{74}$$

with $\varepsilon_r = (1 + \chi)$ being the relative permittivity of the dielectric material. The minimum value of ε_r is unity for vacuum. Its value varies from near unity for most gases to about 80 for water. Substituting for the electric field from Eq. (61), Eq. (73) becomes

$$\nabla^2 \psi = -\frac{\rho_f}{\varepsilon} \tag{75}$$

Equation (75) represents the Poisson's equation for the electric potential distribution in a dielectric material.

3.1.2 Electric double layer

Generally, most substances will acquire a surface electric charge when brought into contact with an electrolyte medium. The magnitude and the sign of this charge depend on the physical properties of the surface and solution. The effect of any charged surface in an electrolyte solution will be to influence the distribution of nearby ions in the solution, and the outcome is the formation of an electric double layer (EDL). The electric double layer, which is shown in Fig. 11, is a region close to the charged surface in which there is an excess of counterions over coions to neutralize the surface charge. The EDL consists of an inner layer known as Stern layer and an outer diffuse layer. The plane separating the inner layer and outer diffuse layer is called the Stern plane. The potential at this plane, ψ_S, is close to the

electrokinetic potential or zeta (ζ) potential, which is defined as the potential at the shear surface between the charged surface and the electrolyte solution. Electrophoretic potential measurements give the zeta potential of a surface. Although one at times refers to a "surface potential", strictly speaking, it is the zeta potential that needs to be specified (Masliyah and Bhattacharjee, 2006). The shear surface itself is somewhat arbitrary but characterized as the plane at which the mobile portion of the diffuse layer can slip or flow past the charged surface (Probstein, 1994).
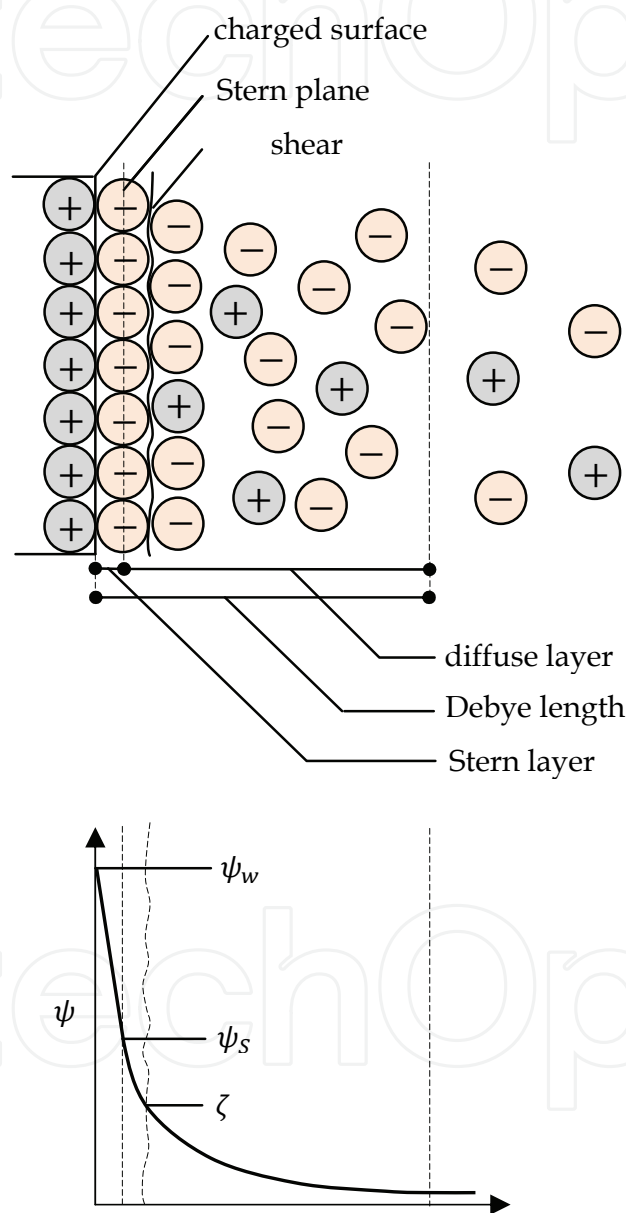
Fig. 11. Structure of electric double layer

The spatial distribution of the ions in the diffuse layer may be related to the electrostatic potential using Boltzmann distribution. It should be pointed out that the Boltzmann distribution assumes the thermodynamic equilibrium, implying that it may be no longer valid in the presence of the fluid flow. However, in most electrokinetic applications, the Peclet number is relatively low, suggesting that using this distribution does not lead to

significant error. At a thermodynamic equilibrium state, the probability that the system energy is confined within the range W and $W + dW$ is proportional to dW, and can be expressed as $\mathcal{P}(W)dW$ with $\mathcal{P}(W)$ being the probability density, given by

$$\mathcal{P} \propto e^{\left(-\frac{W}{k_B T}\right)} \tag{76}$$

where T is the absolute temperature and $k_B = 1.38 \times 10^{-23}$ J/K is the Boltzmann constant. Equation (76), initially derived by Boltzmann, follows from statistical considerations.

Here, W corresponds to a particular location of an ion relative to a suitable reference state. An appropriate choice may be the work W required to bring one ion of valence z_i from infinity, at which $\psi = 0$, to a given location r having a potential ψ. This ion, therefore, possess a charge of $z_i e$ with $e = 1.6 \times 10^{-19}$C being the proton charge. Consequently, the system energy will be $z_i e \psi$ and, as a result, the probability density of finding an ion at location x will be

$$\mathcal{P} \propto e^{\left(-\frac{z_i e \psi}{k_B T}\right)} \tag{77}$$

Similarly, the probability density of finding the ion at the neutral state at which $\psi = 0$ is

$$\mathcal{P}_0 \propto e^{(0)} \tag{78}$$

The ratio of $\mathcal{P}$ to $\mathcal{P}_0$ is taken as being equal to the ratio of the concentrations of the species i at the respective states. Combining Eqs. (77) and (78) results in

$$n_i = n_{i\infty} e^{\left(-\frac{z_i e \psi}{k_B T}\right)} \tag{79}$$

where $n_{i\infty}$ is the ionic concentration at the neutral state and n_i is the ionic concentration of the ith ionic species at the state where the electric potential is ψ. The valence number z_i can be either positive or negative depending on whether the ion is a cation or an anion, respectively. As an example, for the case of CaCl$_2$ salt, z for the calcium ion is +2 and it is −1 for the chloride ion.

We are now ready to investigate the potential distribution throughout the EDL. The charge density of the free ions, ρ_f, can be written in terms of the ionic concentrations and the corresponding valances as

$$\rho_f = \sum_{i=1}^{N} z_i e n_i = \sum_{i=1}^{N} z_i e n_{i\infty} e^{\left(-\frac{z_i e \psi}{k_B T}\right)} \tag{80}$$

For the sake of simplicity, it is assumed that the liquid contains a single salt dissociating into cationic and anionic species, i.e., $N = 2$. It is also assumed that the salt is symmetric implying that both the cations and anions have the same valences, i.e.,

$$z_+ = -z_- = z \tag{81}$$

The charge density, thus, will be of the following form

$$\rho_f = z_+ e n_+ + z_- e n_- = z e n_\infty e^{\left(-\frac{z e \psi}{k_B T}\right)} - z e n_\infty e^{\left(\frac{z e \psi}{k_B T}\right)} \tag{82}$$

or

$$\rho_f = -2zen_\infty \sinh\left(\frac{ze\psi}{k_B T}\right) \tag{83}$$

in which $n_{+\infty} = n_{-\infty} = n_\infty$. Let us know consider the parallel plate microchannel which was shown in Fig. 2. By introducing Eq. (83) into the Poisson's equation, given by Eq. (75), the following differential equation is obtained for the electrostatic potential

$$\frac{\mathrm{d}^2\psi}{\mathrm{d}y^2} = -\frac{2zen_\infty}{\varepsilon}\sinh\left(\frac{ze\psi}{k_B T}\right) \tag{84}$$

The above nonlinear second order one dimensional equation is known as Poisson-Boltzmann equation. Yang et al. (1998) have shown with extensive numerical simulations that the effect of temperature on the potential distribution is negligible. Therefore, the potential field and the charge density may be calculated on the basis of an average temperature, T_{av}. Using this assumption, Eq. (84) in the dimensionless form becomes

$$\frac{\mathrm{d}^2\psi^*}{\mathrm{d}y^{*2}} = \frac{2n_\infty e^2 z^2}{\varepsilon k_B T_{av}} H^2 \sinh\psi^* \tag{85}$$

where $\psi^* = ez\psi/k_B T_{av}$ and $y^* = y/H$. The quantity $(2n_\infty e^2 z^2/\varepsilon k_B T_{av})^{-1/2}$ is the so-called Debye length, λ_D, which characterizes the EDL thickness. It is noteworthy that the general expression for the Debye length is written as $\left(2e^2 \sum_{i=1}^{N} n_{i\infty} z_i^2/\varepsilon k_B T_{av}\right)^{-1/2}$. Defining Debye-Huckel parameter as $\kappa = 1/\lambda_D$, we come up with

$$\frac{\mathrm{d}^2\psi^*}{\mathrm{d}y^{*2}} - \kappa^2 H^2 \sinh\psi^* = 0 \tag{86}$$

If ψ^* is small enough, namely $\psi^* \leq 1$, the term $\sinh\psi^*$ can be approximated by ψ^*. This linearization is known as Debye-Huckel linearization. It is noted that for typical values of $T_{av} = 298K$ and $z = 1$, this approximation is valid for $\psi \leq 25.7\mathrm{mV}$. Defining dimensionless Debye-Huckel parameter, $K = \kappa H$, and invoking Debye-Huckel linearization, Eq. (86) becomes

$$\frac{\mathrm{d}^2\psi^*}{\mathrm{d}y^{*2}} - K^2\psi^* = 0 \tag{87}$$

The boundary conditions for the above equation are

$$\left(\frac{\mathrm{d}\psi^*}{\mathrm{d}y^*}\right)_{(0)} = 0 \quad , \quad \psi^*_{(1)} = \zeta^* \tag{88}$$

in which ζ^* is the dimensionless wall zeta potential, i.e., $\zeta^* = ez\zeta/k_B T_{av}$. Using Eq. (87) and applying boundary conditions (88), the dimensionless potential distribution is obtained as follows

$$\psi^* = \zeta^* \frac{\cosh{(Ky^*)}}{\cosh K} \tag{89}$$

Figure 12 shows the transverse distribution of ψ^* at different values of ζ^*. The simplified cases are those pertinent to the Debye-Huckel linearization and the exact ones are the results of the Numerical solution of Eq. (86). The figure demonstrates that performing the Debye-Huckel linearization does not lead to significant error up to $\zeta^* \cong 2$ which corresponds to the value of about 51.4 mV for the zeta potential at standard conditions. This is due to the fact that for $\zeta^* = 2$, the dimensionless potential is lower than 1 over much of the duct cross section. According to Karniadakis et al. (2005), the zeta potential range for practical applications is $1 - 100$ mV, implying that the Debye-Huckel linearization may successfully be used to more than half of the practical applications range of the zeta potential.
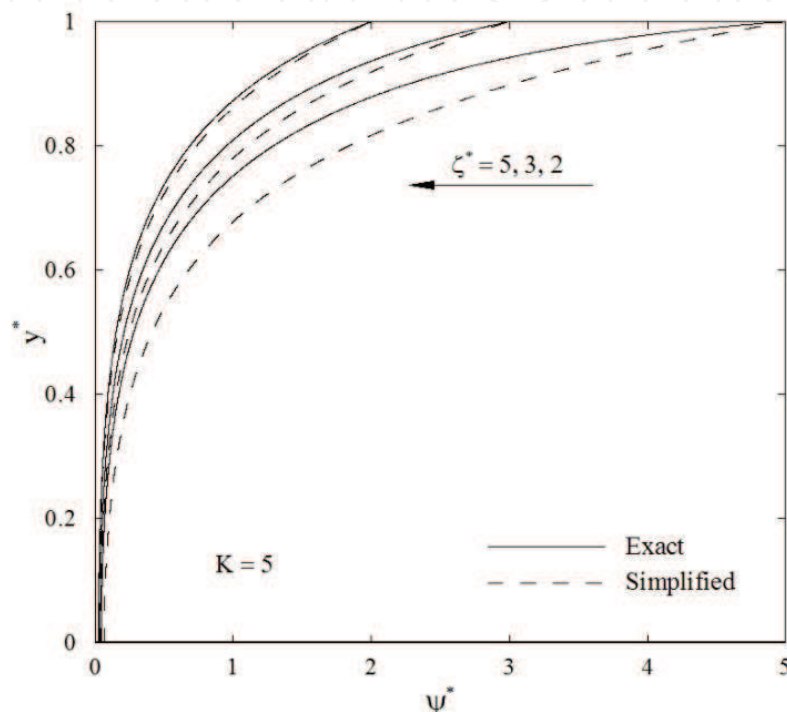
Fig. 12. Transverse distribution of ψ^* at different values of ζ^*

3.2 Electroosmosis

As mentioned previously, there is an excess of counterions over coions throughout the EDL. Suppose that the surface charge is negative, as shown in Fig. 13. If one applies an external electric field, the outcome will be a net migration toward the cathode of ions in the surface liquid layer. Due to viscous drag, the liquid is drawn by the ions and therefore flows through the channel. This is referred to as electroosmosis. Electroosmosis has many applications in sample collection, detection, mixing and separation of various biological and chemical species. Another and probably the most important application of electroosmosis is the fluid delivery in microscale at which the electroosmotic micropump has many advantages over other types of micropumps. Electroosmotic pumps are bi directional, can generate constant and pulse free flows with flow rates well suited to microsystems and can be readily integrated with lab on chip devices. Despite various advantages of the electroosmotic pumping systems, the pertinent Joule heating is an unfavorable phenomenon. Therefore, a pressure driven pumping system is sometimes added to the electroosmotic pumping systems in order to reduce the Joule heating effects, resulting in a combined electroosmotically and pressure driven pumping.
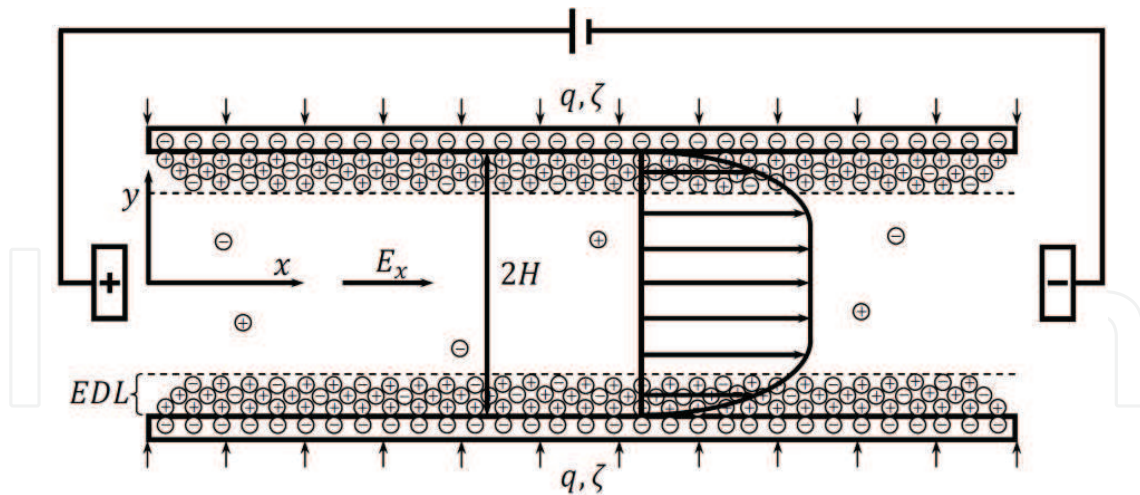
Fig. 13. A parallel plate microchannel with an external electric field

In the presence of external electric field, the poison equation becomes

$$\nabla^2 \varphi = -\frac{\rho_f}{\varepsilon} \tag{90}$$

The potential φ is now due to combination of externally imposed field Φ and EDL potential ψ, namely

$$\varphi = \Phi + \psi \tag{91}$$

For a constant voltage gradient in the x direction, Eq. (90) is reduced to Eq. (84), and thus the potential distribution is again given by Eq. (89). The momentum exchange through the flow field is governed by the Cauchy's equation given as

$$\rho \frac{D\mathbf{u}}{Dt} = -\nabla p + \nabla \cdot \boldsymbol{\tau} + \mathbf{F} \tag{92}$$

in which p represents the pressure, $\mathbf{u}$ and $\mathbf{F}$ are the velocity and body force vectors, respectively, and $\boldsymbol{\tau}$ is the stress tensor. The body force is given by (Masliyah and Bhattacharjee, 2006)

$$\mathbf{F} = \rho_f \mathbf{E} - \frac{1}{2}\mathbf{E} \cdot \mathbf{E}\nabla\varepsilon + \frac{1}{2}\nabla\left[\left(\rho \frac{\partial\varepsilon}{\partial\rho}\right)_T \mathbf{E} \cdot \mathbf{E}\right] \tag{93}$$

Therefore, for the present case, the body force is reduced to $\rho_f E_x$, assuming a medium with constant permittivity. Regarding that $D\mathbf{u}/Dt = 0$ at fully developed conditions, we come up with the following expression for the momentum equation in the x direction

$$\mu \frac{d^2 u}{dy^2} = \frac{dp}{dx} + 2E_x n_0 ez \sinh\left(\frac{ez\psi}{k_B T_{av}}\right) \tag{94}$$

Invoking the Debye-Huckel linearization, the dimensionless form of the momentum equation becomes

$$\frac{d^2 u^*}{dy^{*2}} = -2\Gamma - \frac{K^2}{\zeta^*}\psi^* = -2\Gamma - K^2 \frac{\cosh(Ky^*)}{\cosh K} \tag{95}$$

in which $u^* = u/u_{HS}$ with $u_{HS} = -\varepsilon\zeta E_x/\mu$ being the maximum possible electroosmotic velocity for a given applied potential field, known as the Helmholtz-Smoluchowski

electroosmotic velocity. It is noteworthy that $\varepsilon\zeta/\mu$ is often termed the electroosmotic mobility of the liquid. Also Γ is the ratio of the pressure driven velocity scale to u_{HS}, namely $\Gamma = u_{PD}/u_{HS}$ where $u_{PD} = -H^2(\mathrm{d}p/\mathrm{d}x)/2\mu$. The boundary conditions for the momentum equation are the symmetry condition at centerline and no slip condition at the wall. The dimensionless velocity profile then is readily obtained as

$$u^* = \Gamma\left(1 - y^{*2}\right) + 1 - \frac{\cosh\left(Ky^*\right)}{\cosh K} \tag{96}$$

Dimensionless velocity profile for purely electroosmotic flow is depicted in Fig. 14. For a sufficiently small value of K such as $K = 1$, since EDL potential distribution over the duct cross section is nearly uniform which is the source term in momentum equation (94), so the velocity distribution is similar to Poiseuille flow. As dimensionless Debye-Huckel parameter increases the dimensionless velocity distribution shows a behavior which is different from Poiseuille flow limiting to a slug flow profile at sufficiently great values of K. This is due to the fact that at higher values of K, the body force is concentrated in the region near the wall.
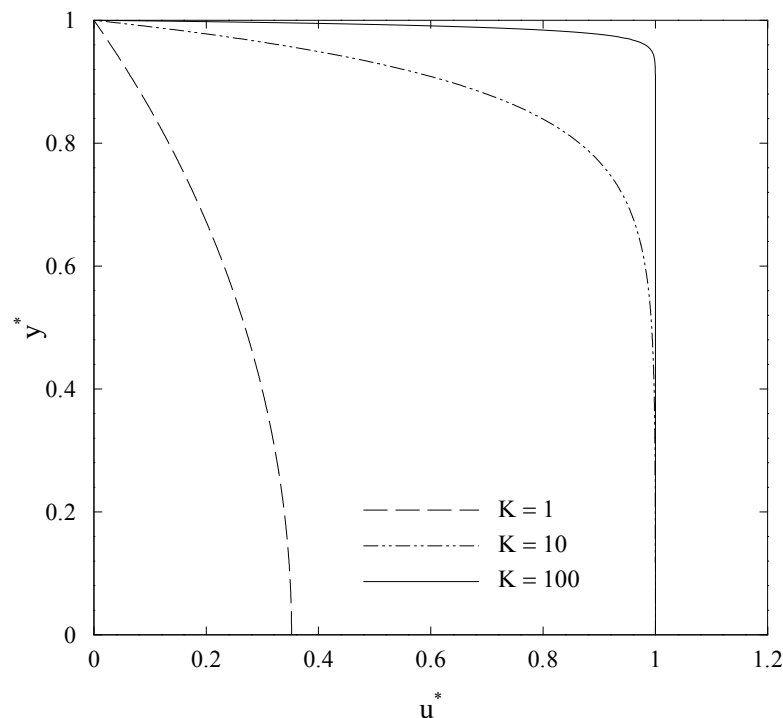

Fig. 14. Dimensionless velocity profile for purely electroosmotic flow

Dimensionless velocity profile at different values of Γ at $K = 100$ is illustrated in Fig. 15. As observed, the velocity profile for non zero values of Γ is the superposition of both purely electroosmotic and Poiseuille flows. Note that for sufficiently large amounts of the opposed pressure, reverse flow may occur at centerline.

Electrokinetic flow in ultrafine capillary slits was firstly analyzed by Burgreen and Nakache (1964). Rice and Whitehead (1965) investigated fully developed electroosmotic flow in a narrow cylindrical capillary for low zeta potentials, using the Debye-Huckel linearization. Levine et al. (1975) extended the Rice and Whitehead's work to high zeta potentials by means of an approximation method. More recently, an analytical solution for electroosmotic flow in a cylindrical capillary was derived by Kang et al. (2002a) by solving the complete

Poisson-Boltzmann equation for arbitrary zeta potentials. They (2002b) also analytically analyzed electroosmotic flow through an annulus under the situation when the two cylindrical walls carry high zeta potentials. Hydrodynamic characteristics of the fully developed electroosmotic flow in a rectangular microchannel were reported in a numerical study by Arulanandam and Li (2000).
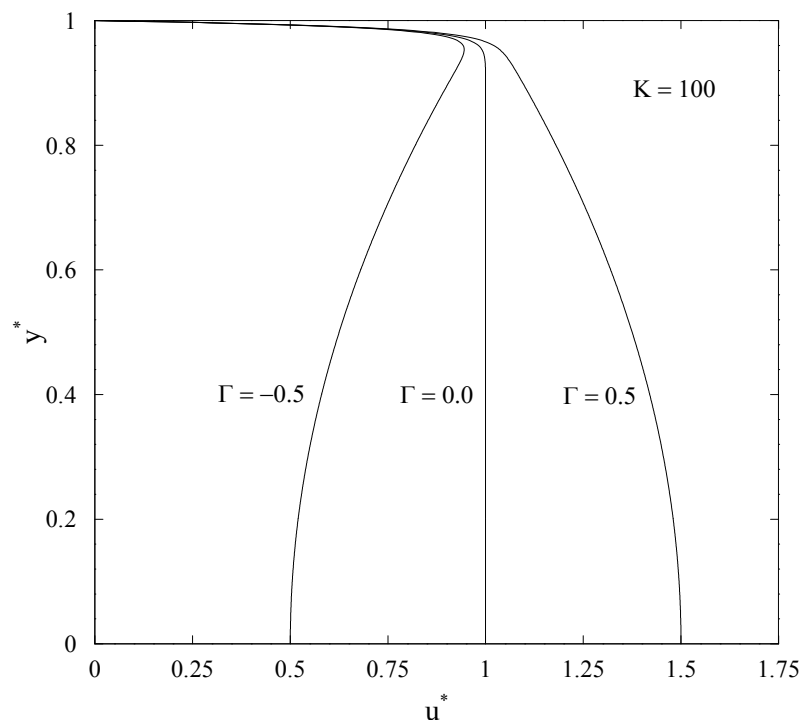

Fig. 15. Dimensionless velocity profile at different values of Γ

Let us now pay attention to the thermal features. Note that the passage of electrical current through the liquid generates a volumetric energy generation known as Joule heating. The conservation of energy including the effect of Joule heating requires

$$\rho c_p \frac{DT}{Dt} = \nabla \cdot (k\nabla T) + s \tag{97}$$

In the above equation, s denotes the rate of volumetric heat generation due to Joule heating and equals $s = E_x^2/\sigma$ with σ being the liquid electrical resistivity given by (Levine et al., 1975)

$$\sigma = \frac{\sigma_0}{\cosh\left(\frac{ez\psi}{k_B T_{av}}\right)} \tag{98}$$

in which σ_0 is the electrical resistivity of the neutral liquid. The hyperbolic term in the above equation accounts for the fact that the resistivity within the EDL is lower than that of the neutral liquid, due to an excess of ions close to the surface. For low zeta potentials, which is assumed here, $\cosh(ez\psi/k_B T_{av}) \to 1$ and, as a result, the Joule heating term may be considered as the constant value of $s = E_x^2/\sigma_0$. For steady fully developed flow $DT/Dt = u(\partial T/\partial x)$, so energy equation (97) becomes

$$\rho c_p u \frac{\partial T}{\partial x} = k\left(\frac{\partial^2 T}{\partial x^2} + \frac{\partial^2 T}{\partial y^2}\right) + \frac{E_x^2}{\sigma_0} \tag{99}$$

and in dimensionless form

$$\frac{\mathrm{d}^2\theta}{\mathrm{d}y^{*2}} = (1+S)\frac{u^*}{u_m^*} - S \tag{100}$$

with the following dimensionless variables for a constant wall heat flux of q

$$\theta(y) = \frac{T-T_w}{\frac{qH}{k}} \quad , \quad S = \frac{E_x^2 H}{q\sigma_0} \quad , \quad u_m^* = \int_0^1 u^* \mathrm{d}y^* = 1 + \frac{2}{3}\Gamma - \frac{\tanh K}{K} \tag{101}$$

The corresponding non-dimensional boundary conditions for the energy equation are

$$\left(\frac{\mathrm{d}\theta}{\mathrm{d}y^*}\right)_{(0)} = 0 \quad , \quad \theta_{(1)} = 0 \tag{102}$$

The solution of Eq. (100) subject to boundary conditions (102) may be written as

$$\theta = \left[(1+\Gamma)\frac{1+S}{u_m^*} - S\right]\frac{y^{*2}}{2} - \frac{\Gamma(1+S)}{12u_m^*}y^{*4} - \frac{(1+S)}{u_m^*}\frac{\cosh(Ky^*)}{K^2\cosh K} + a \tag{103}$$

in which

$$a = \left(\frac{1}{K^2} - \frac{1}{2} - \frac{5}{12}\Gamma\right)\frac{1+S}{u_m^*} + \frac{S}{2} \tag{104}$$

The dimensionless mean temperature is given by

$$\theta_b = \frac{\int_0^1 u^*\theta \mathrm{d}y^*}{\int_0^1 u^*\mathrm{d}y^*} = \frac{\int_0^1 u^*\theta \mathrm{d}y^*}{u_m^*} \tag{105}$$

and the Nusselt number will be

$$Nu = \frac{hD_h}{k} = \frac{qD_h}{k(T_w - T_b)} = -\frac{4}{\theta_b} \tag{106}$$

The complete expression for the Nusselt number is given by Chen (2009) and it is

$$Nu = c_4 u_m^* \tag{107}$$

where

$$\begin{aligned}
c_4^{-1} = &\frac{1}{210}\left\{14\left[10c_1 + 12c_2 + 15c_3 - \frac{30}{K^2}(c_1 + 2c_2) - \frac{360}{K^4}c_2\right]\right. \\
&+ 4\left[28c_1 + 32c_2 + 35c_3\left(1 - \frac{3}{K^2}\right)\right]\Gamma\right\} \\
&+ \frac{1}{2}\left\{c_3\,\mathrm{sech}^2 K + \frac{\tanh K}{K}\left[\frac{4}{K^2}\left(c_1 + 6c_2 + 12\frac{c_2}{K^2}\right) - c_3\left(3 - 4\frac{\Gamma}{K^2}\right)\right]\right\}
\end{aligned} \tag{108}$$

with the following coefficients

$$c_1 = \frac{1}{8}\left[(1+\Gamma)\frac{1+S}{u_m^*} - S\right] \quad , \quad c_2 = -\Gamma\frac{1+S}{48u_m^*} \quad , \quad c_3 = -\frac{1+S}{4u_m^*K^2} \tag{109}$$

Figure 16 depicts the Nusselt number values versus $1/K$ for purely electroosmotic flow. It can be seen that to increase S is to decrease Nusselt number. Increasing the Joule heating effects results in more accumulation of energy near the wall and, consequently, higher wall temperatures. The ultimate outcome thus will be smaller values of Nusselt number, according to Eq. (106). As K goes to infinity, for all values of S, the Nusselt number approaches 12 which is the classical solution for slug flow (Burmeister, 1993).
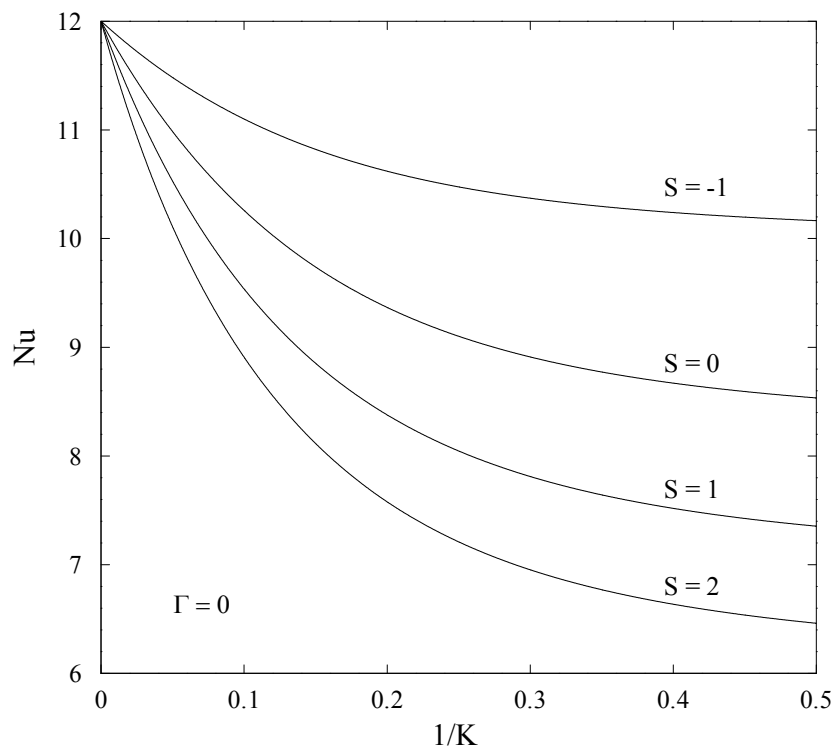
Fig. 16. Nusselt number versus $1/K$ for purely electroosmotic flow

Unlike hydrodynamic features, the study of thermal features of electroosmosis is recent. Maynes and Webb (2003) were the first who considered the thermal aspects of the electroosmotic flow due to an external electric field. They analytically studied fully developed electroosmotically generated convective transport for a parallel plate microchannel and circular microtube under imposed constant wall heat flux and constant wall temperature boundary conditions. Liechty et al. (2005) extended the above work to the high zeta potentials. It was determined that elevated values of wall zeta potential produce significant changes in the charge potential, electroosmotic flow field, temperature profile, and Nusselt number relative to previous results invoking the Debye-Huckel linearization. Also thermally developing electroosmotically generated flow in circular and rectangular microchannels have been considered by Broderick et al. (2005) and Iverson et al. (2004), respectively. The effect of viscous dissipation in fully developed electroosmotic heat transfer for a parallel plate microchannel and circular microtube under imposed constant wall heat flux and constant wall temperature boundary conditions was analyzed by Maynes and Webb (2004). In a recent study, Sadeghi and Saidi (2010) derived analytical solutions for thermal features of combined electroosmotically and pressure driven flow in a slit microchannel, by taking into account the effects of viscous heating.

3.3 Streaming potential

The EDL effects may be present even in the absence of an externally applied electric field. Consider the pressure driven flow of an ionized liquid in a channel with negatively charged surface. According to the Boltzmann distribution, there will be an excess of positive ions over negative ions in liquid. The ultimate effect thus will be an electrical current due to the liquid flow, called the streaming current, I_s. According to the definition of electrical current, the streaming current is of the form

$$I_s = \int u\rho_f \, \mathrm{d}A \tag{110}$$

where A is the channel cross sectional are and u is the streamwise velocity. The streaming current accumulates positive ions at the end of the channel. Consequently, a potential difference, called the streaming potential, Φ_s, is created between the two ends of the channel. The streaming potential generates the so-called conduction current, I_c, which carries charges and molecules in the opposite direction of the flow, creating extra impedance to the flow motion. The net electrical current, I, is the sum of the streaming current and the conduction current and in steady state should be zero

$$I = I_s + I_c = 0 \tag{111}$$

In order to study the effects of the EDL on a pressure driven flow, first the conduction current should be evaluated from Eqs. (110) and (111). Afterwards, the value of I_c is used to find out the electric field associated with the flow induced potential, E_s, using the following relationship

$$E_s = \frac{I_c\sigma}{A} \tag{112}$$

The flow induced electric field then is used to evaluate the body force in the momentum equation. It should be pointed out that since there is not any electrical current due to an external electric field, therefore, the Joule heating term does not appear in the energy equation.

4. References

Arulanandam, S. & Li, D. (2000). Liquid transport in rectangular microchannels by electroosmotic pumping. *Colloids and Surfaces A: Physicochemical and Engineering Aspects*, Vol. 161, pp. 89–102, 0927-7757

Aydin, O. & Avci, M. (2006). Heat and flow characteristics of gases in micropipes, *Int. J. Heat Mass Transfer*, Vol. 49, pp. 1723–1730, 0017-9310

Aydin, O. & Avci, M. (2007). Analysis of laminar heat transfer in micro-Poiseuille flow, *Int. J. Thermal Sciences*, Vol.46, pp. 30–37, 1290-0729

Beskok, A. & Karniadakis, G.E. (1994). Simulation of heat and momentum transfer in complex micro-geometries. *J. Thermophysics Heat Transfer*, Vol. 8, pp. 647–655, 0887-8722

Biswal, L.; Som, S.K. & Chakraborty, S. (2007). Effects of entrance region transport processes on free convection slip flow in vertical microchannels with isothermally heated walls. *Int. J. Heat Mass Transfer*, Vol. 50, pp. 1248–1254, 0017-9310

Broderick, S.L.; Webb, B.W. & Maynes, D. (2005). Thermally developing electro-osmotic convection in microchannels with finite Debye-layer thickness. *Numerical Heat Transfer, Part A*, Vol. 48, pp. 941–964, 1040-7782

Burgreen, D. & Nakache, F.R. (1964). Electrokinetic flow in ultrafine capillary slits. *J. Physical Chemistry*, Vol. 68, pp. 1084–1091, 1089-5639

Burmeister, L.C. (1993). *Convective heat transfer*, Wiley, 0471310204, New York

Chakraborty, S.; Som, S.K. & Rahul (2008). A boundary layer analysis for entrance region heat transfer in vertical microchannels within the slip flow regime. *Int. J. Heat Mass Transfer*, Vol. 51, pp. 3245–3250, 0017-9310

Chen, C.K. & Weng, H.C. (2005). Natural convection in a vertical microchannel. *J. Heat Transfer*, Vol. 127, pp. 1053–1056, 0022-1481

Chen, C.H. (2009). Thermal transport characteristics of mixed pressure and electroosmotically driven flow in micro- and nanochannels with Joule heating. *J. Heat Transfer*, Vol. 131, 022401, 0022-1481

Hadjiconstantinou, N.G. (2003). Dissipation in small scale gaseous flows. *J. Heat Transfer,* Vol. 125, pp. 944-947, 0022-1481

Hadjiconstantinou, N.G. (2006). The limits of Navier Stokes theory and kinetic extensions for describing small scale gaseous hydrodynamics. *Phys. Fluids*, Vol. 18, 111301, 1070-6631

Iverson, B.D.; Maynes, D. & Webb, B.W. (2004). Thermally developing electroosmotic convection in rectangular microchannels with vanishing Debye-layer thickness. *J. Thermophysics Heat Transfer*, Vol. 18, pp. 486–493, 0887-8722

Jeong, H.E. & Jeong, J.T. (2006a). Extended Graetz problem including axial conduction and viscous dissipation in microtube, *J. Mechanical Science Technology,* Vol. 20, pp. 158–166, 1976-3824

Jeong, H.E. & Jeong, J.T. (2006b). Extended Graetz problem including streamwise conduction and viscous dissipation in microchannel, *Int. J. Heat Mass Transfer,* Vol. 49, pp. 2151–2157, 0017-9310

Kandlikar, S.G.; Garimella, S.; Li, D.; Colin, S. & King, M.R. (2006). *Heat Transfer and Fluid Flow in Minichannels and Microchannels*, Elsevier, 0-0804-4527-6, Oxford

Kang, Y.; Yang, C. & Huang, X. (2002a). Dynamic aspects of electroosmotic flow in a cylindrical microcapillary. *Int. J. Engineering Science*, Vol. 40, pp. 2203–2221, 0020-7225

Kang, Y.; Yang, C. & Huang, X. (2002b). Electroosmotic flow in a capillary annulus with high zeta potentials. *J. Colloid Interface Science*, Vol. 253, pp. 285–294, 0021-9797

Karniadakis, G.; Beskok, A. & Aluru, N. (2005). *Microflows and Nanoflows, Fundamentals and Simulation*, Springer, 0-387-90819-6, New York

Kennard, E.H. (1938). *Kinetic Theory of Gases*, McGraw–Hill, New York

Koo, J. & Kleinstreuer, C. (2003). Liquid flow in microchannels: experimental observations and computational analyses of microfluidics effects. *J. Micromechanics and Microengineering,* Vol. 13, pp. 568–579, 1361-6439

Koo, J. & Kleinstreuer, C. (2004). Viscous dissipation effects in microtubes and microchannels, *Int. J. Heat Mass Transfer,* Vol. 47, pp. 3159–3169, 0017-9310

Levine, S.; Marriott, J.R.; Neale, G. & Epstein, N. (1975). Theory of electrokinetic flow in fine cylindrical capillaries at high zeta-potentials. *J. Colloid Interface Science*, Vol. 52, 136–149, 0021-9797

Liechty, B.C.; Webb, B.W. & Maynes, R.D. (2005). Convective heat transfer characteristics of electro-osmotically generated flow in microtubes at high wall potential. *Int. J. Heat Mass Transfer*, Vol. 48, pp. 2360–2371, 0017-9310

Masliyah J.H. & Bhattacharjee, S. (2006). *Electrokinetic and Colloid Transport Phenomena*, First ed., John Wiley, 0-471-78882-1, New Jersey.

Maxwell, J.C. (1879). On stresses in rarefied gases arising from inequalities of temperature, *Philos. Trans. Royal Soc.*, Vol. 170, pp. 231-256

Maynes, D. & Webb, B.W. (2003). Fully developed electroosmotic heat transfer in microchannels. *Int. J. Heat Mass Transfer*, Vol. 46, pp. 1359–1369, 0017-9310

Maynes, D. & Webb, B.W. (2004). The effect of viscous dissipation in thermally fully developed electroosmotic heat transfer in microchannels. *Int. J. Heat Mass Transfer*, Vol. 47, pp. 987–999, 0017-9310

Niazmand, H.; Jaghargh, A.A. & Renksizbulut, M. (2010). Slip-flow and heat transfer in isoflux rectangular microchannels with thermal creep effects. *J. Applied Fluid Mechanics*, Vol. 3, pp. 33-41, 1735-3645

Ou, J.W. & Cheng, K.C. (1973). Effects of flow work and viscous dissipation on Graetz problem for gas flows in parallel-plate channels, *Heat Mass Transfer*, Vol. 6, pp. 191–198, 0947-7411

Probstein, R.F. (1994). *Physicochemical Hydrodynamics*, 2nd ed. Wiley, 0471010111, New York

Rice, C.L. & Whitehead, R. (1965). Electrokinetic flow in a narrow cylindrical capillary. *J. Physical Chemistry*, Vol. 69, pp. 4017–4024, 1089-5639

Rij, J.V.; Harman, T. & Ameel, T. (2007). The effect of creep flow on two-dimensional isoflux microchannels. *Int. J. Thermal Sciences*, Vol. 46, pp. 1095–1103, 1290-0729

Rij, J.V.; Ameel, T. & Harman, T. (2009). The effect of viscous dissipation and rarefaction on rectangular microchannel convective heat transfer. *Int. J. Thermal Sciences,* Vol. 48, pp. 271–281, 1290-0729

Sadeghi, A.; Asgarshamsi, A. & Saidi M.H. (2009). Analysis of laminar flow in the entrance region of parallel plate microchannels for slip flow, *Proceedings of the Seventh International ASME Conference on Nanochannels, Microchannels and Minichannels, ICNMM2009,* S.G. Kandlikar (Ed.), Pohang, South Korea

Sadeghi, A. & Saidi, M.H. (2010). Viscous dissipation and rarefaction effects on laminar forced convection in microchannels. *J. Heat Transfer,* Vol. 132, 072401, 0022-1481

Sadeghi, A. & Saidi, M.H. (2010). Viscous dissipation effects on thermal transport characteristics of combined pressure and electroosmotically driven flow in microchannels. *Int. J. Heat Mass Transfer*, Vol. 53, pp. 3782–3791, 0017-9310

Taheri, P.; Torrilhon, M. & Struchtrup, H. (2009). Couette and Poiseuille microflows: analytical solutions for regularized 13-moment equations. *Phys. Fluids*, Vol. 21, 017102, 1070-6631

Tunc, G.& Bayazitoglu, Y. (2002). Heat transfer in rectangular microchannels. *Int. J. Heat Mass Transfer*, Vol. 45, pp. 765–773, 0017-9310

Weng, H.C. & Chen, C.K. (2008a). On the importance of thermal creep in natural convective gas microflow with wall heat fluxes. *J. Phys. D*, Vol. 41, 115501, 0022-3727

Weng, H.C. & Chen, C.K. (2008b). Variable physical properties in natural convective gas microflow. *J. Heat Transfer*, Vol. 130, 082401, 0022-1481

Yang, C.; Li, D. & Masliyah, J.H. (1998). Modeling forced liquid convection in rectangular microchannels with electrokinetic effects. *Int. J. Heat Mass Transfer*, Vol. 41, pp. 4229–4249, 0017-9310

Yu, S. & Ameel, T.A. (2001). Slip flow heat transfer in rectangular microchannels. *Int. J. Heat Mass Transfer*, Vol. 44, pp. 4225–4234, 0017-9310
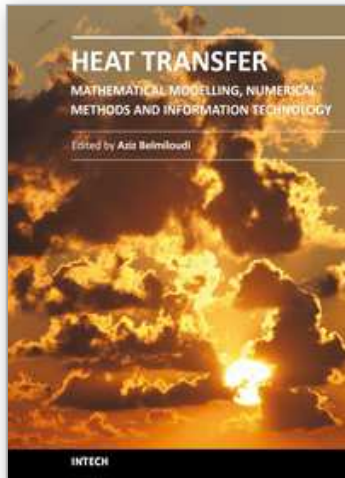
Heat Transfer - Mathematical Modelling, Numerical Methods and Information Technology
Edited by Prof. Aziz Belmiloudi

Over the past few decades there has been a prolific increase in research and development in area of heat transfer, heat exchangers and their associated technologies. This book is a collection of current research in the above mentioned areas and describes modelling, numerical methods, simulation and information technology with modern ideas and methods to analyse and enhance heat transfer for single and multiphase systems. The topics considered include various basic concepts of heat transfer, the fundamental modes of heat transfer (namely conduction, convection and radiation), thermophysical properties, computational methodologies, control, stabilization and optimization problems, condensation, boiling and freezing, with many real-world problems and important modern applications. The book is divided in four sections : "Inverse, Stabilization and Optimization Problems", "Numerical Methods and Calculations", "Heat Transfer in Mini/Micro Systems", "Energy Transfer and Solid Materials", and each section discusses various issues, methods and applications in accordance with the subjects. The combination of fundamental approach with many important practical applications of current interest will make this book of interest to researchers, scientists, engineers and graduate students in many disciplines, who make use of mathematical modelling, inverse problems, implementation of recently developed numerical methods in this multidisciplinary field as well as to experimental and theoretical researchers in the field of heat and mass transfer.

How to reference
In order to correctly reference this scholarly work, feel free to copy and paste the following:

INTECH
open science | open minds

www.intechopen.com